Fatigue Performance of Bearing Rollers Manufactured by Laser Powder Bed Fusion

Luz D. Sotelo[1,4], Allen J. Fuller[2], Cody S. Pratt[1], Guru Madireddy[1,3], Rakeshkumar Karunakaran[1,4], Michael P. Sealy[1,4], Timothy M. Liebe[2] and Joseph A. Turner[1]

ABSTRACT

Metal additive manufacturing (AM) promises functional flexibility for the production of engineering components and great progress has been made with respect to part geometry and overall performance criteria. Fracture and fatigue behavior of metals are inherently dependent on the sample microstructure, an aspect of metal AM for which many challenges remain. Here, we report on progress with respect to the rolling contact fatigue (RCF) performance of metal AM bearing rollers. A set of rollers was created using laser powder bed fusion from 8620HC steel powder. The print parameters were first studied with respect to laser power, laser scan speed, laser spot size, and layer thickness. A set of tapered cylindrical rollers was then manufactured using build parameters that were selected based on material density, optical microscopy, ultrasound, and residual stress measurements. The rollers were then heat treated while still on the build plate to relieve any residual stresses. The rollers were removed from the build plate, machined to the typical product geometry, case hardened, carburized, and ground to a final surface finish. Finally, the rollers were integrated within railroad tapered roller bearings and tested in two ways. The accelerated life test subjected the rollers to high stress RCF that generated significant spalling on both types of rollers. The simulated service life test was designed with RCF at levels typical of in-

[1]Mechanical and Materials Engineering, University of Nebraska-Lincoln, Lincoln, NE, USA.
[2]Amsted Rail Brenco, 2580 Frontage Road, Petersburg Industrial Park, Petersburg, VA 23805, USA
[3]Current affiliation: Manufacturing Science Division, Oak Ridge National Lab, Oak Ridge, TN, USA
[4]Current affiliation: School of Mechanical Engineering, Purdue University, West Lafayette, IN, 47907 USA

service bearings. At the conclusion of this test equivalent of 250,000 miles, the performance of the AM rollers was judged to be in-line with rollers manufactured using traditional methods and visual inspections showed no surface damage to any rollers. The results of this study provide a clear foundation for additional AM roller designs that can exploit the unique capabilities of the AM process.

Keywords

railroad bearing, metal additive manufacturing, rolling contact fatigue, bearing spalls, metal 3D printing

INTRODUCTION

Railroad bearings subject to heavy freight loads must be designed and manufactured in order to perform well over the course of the bearing lifetime which often exceeds one million miles [1]. In particular, the quality of the steel used for bearing production must ensure that impurities are not present, especially in the regions of material subjected to the highest stresses. During service, bearings undergo rolling contact fatigue (RCF), and fail due to subsurface fatigue spalls that result from micro-cracks initiated by near-surface defects acting as stress concentrators [2-4]. The production of high-quality steels has greatly reduced the probability of RCF failure for components made using conventional manufacturing methods. However, new manufacturing approaches, based on metal additive manufacturing (AM), are not as well studied with respect to RCF [5 -7] but have disrupted traditional manufacturing design concepts in aerospace, automotive, and biomedical applications [8]. Such a disruption could occur with regard to railroad component production if the resulting materials can meet RCF performance criteria and if the components can be created in a cost-efficient manner.

Metal AM promises increased freedom in the geometry and composition of a component, which facilitates high customization and low batch production [8 -10]. Nonetheless, practical engineering applications for parts manufactured with metal AM are still limited mostly to non-structural components [10]. The uncertainty in mechanical properties due to the stochastic nature of metal AM processes continues to prevent their wide-spread adoption for manufacturing of load-bearing components [8]. While considerable work has been dedicated to study the static mechanical properties of various metal alloys processed via metal AM, their fatigue behavior is far less explored [11]. Additionally, mechanical characterization of metal AM parts is typically limited to a few select alloys and loading conditions [12].

The fatigue behavior of metal AM parts depends on three main factors, namely the static mechanical properties of the part, its surface finish, and its defect content. In general metal AM parts have higher strength than their conventionally manufactured counterparts, due to a more refined microstructure. However, they are also more likely to exhibit anisotropy and a high defect content (e.g. porosity, lack of fusion, micro-cracking) [12], the latter resulting in lower fatigue strength [13]. Previous work has studied the effect of defect content [11-18], surface finish [11-12, 14, 16, 19-22], orientation [13, 20, 23], and stress state [11, 14-15, 17, 24] on the fatigue behavior of metal AM samples. Several studies have found that, of all these factors, surface finish has the greatest impact on fatigue life, with significantly lower life with decreasing surface quality [12]. The effect of defect content depends on the type, geometry, and location of the defects within the sample. For instance, small spherical porosity distributed within the bulk of the sample has little effect on its fatigue life [25-26], while large irregular porosity or inclusions, such as those produced due to lack-of-fusion, significantly affect fatigue behavior, especially when located close to the surface [27-31]. Heat treatment for stress-relieving has also been observed to improve

fatigue performance [26, 32], while the effect of orientation is dependent on the loading conditions [12-13, 21, 23].

Fatigue performance of metal AM samples has been primarily studied under uniaxial loading conditions [11, 15-19, 21, 23, 25-27, 29, 31, 33-35]. Additionally, authors have started to consider fatigue behavior under multiaxial loading such as torsional [20, 28, 36-38], bending [13-14, 22, 24, 30], and rolling contact fatigue testing [5-7]. Of these loading conditions, RCF is by far the least explored. Hassila et al. [5], found different failure modes in AM and conventionally manufactured Inconel 625 cylindrical samples subject to RCF loading. Liu et al. [6] found that ultrasonic surface rolling of AM Ti6Al4V cylindrical samples considerably improved their RCF performance. Finally, Yang et al. [7] found that laser-cladded rail steel samples performed better than their uncoated counterparts during rolling tests with ball elements under dry conditions. They related their experimental findings to finite element simulations wheel-rail RCF. However, understanding of RCF for metal AM components is still limited, and there has been no extensive lifetime RCF testing of fully built mechanical components with metal AM parts.

The objective of this work was to test the performance of additively manufactured metal parts, specifically tapered bearing rollers, subjected to RCF. For this purpose, first a thorough parameter selection process was implemented to optimize process parameters for the application. Then, 50 rollers, hereon denoted as the AM rollers, were additively manufactured from 8620 steel using these process parameters. The AM rollers were postprocessed along with conventionally manufactured (CM) rollers that were used for comparison. Finally, the AM and CM rollers were subjected to two RCF experimental tests and their conditions compared. This work provides clear guidance to application-oriented process parameter development for AM, while the results

presented here are foundational for novel AM roller designs as well as the understanding of RCF in AM components.

PROCESS PARAMETER SELECTION

The selection of process parameters for metal AM is non-trivial as it is both material and geometry dependent [39-41]. In particular, defining AM process parameters for alloys that are atypical to metal AM processes poses an important challenge. While multiple authors have proposed methodologies for metal AM process parameter development [39, 42-45], most of these methods define the parameter space for three-dimensional parts based on one and two-dimensional features. To compensate for this drawback, customary process parameter development practices [39, 43-44] were modified such that the selected parameters were application-oriented. More specifically, the desired component properties were defined first, such that they guided the measurement parameters and importance. Once measurements were completed, the results were quantified in a decision matrix which was then used to finalize the process parameter selection.

The end goal for the components of interest here was to withstand RCF during simulated service life testing. RCF performance of components is affected by microstructural defects, hard inclusions, and porosity which may initiate subsurface micro-cracks. Once initiated, these cracks often propagate towards the surface and create surface cavities (i.e., spalls) which continue to grow until catastrophic failure of the component [46-48]. Thus, the first preferred characteristics defined are uniform microstructure and high part densification. Additionally, the close proximity of the rollers within the AM build volume required low tensile residual stress to avoid print failure which defines another preferred characteristic. Reduction of tensile residual stresses is also relevant to avoid stress induced crack propagation [49].

With the preferred part characteristics defined, the process parameter measurements were established as shown in Fig. 1(a). The raw material powder was assessed to ensure its safe utilization within the LPBF system. Then, a typical melt pool evaluation [39, 43-44] was conducted to test a total of 18 process parameter combinations and create a linear process map that allowed the reduction of the parameter search space to 6 parameter sets. Based on those results, four types of volumetric testing were conducted; namely, short-track evaluation to probe melt pool uniformity, density measurements to find the porosity content, ultrasound measurements to evaluate the microstructure uniformity, and deflection measurements from NIST bridge structures to evaluate residual stresses [50]. The results from this second evaluation stage were used to create a decision matrix and define the manufacturing parameters for the AM rollers. Images of the LPBF process, and relevant build plates and samples for the linear and volumetric parameter tests are shown in Fig 1(b)-(d).
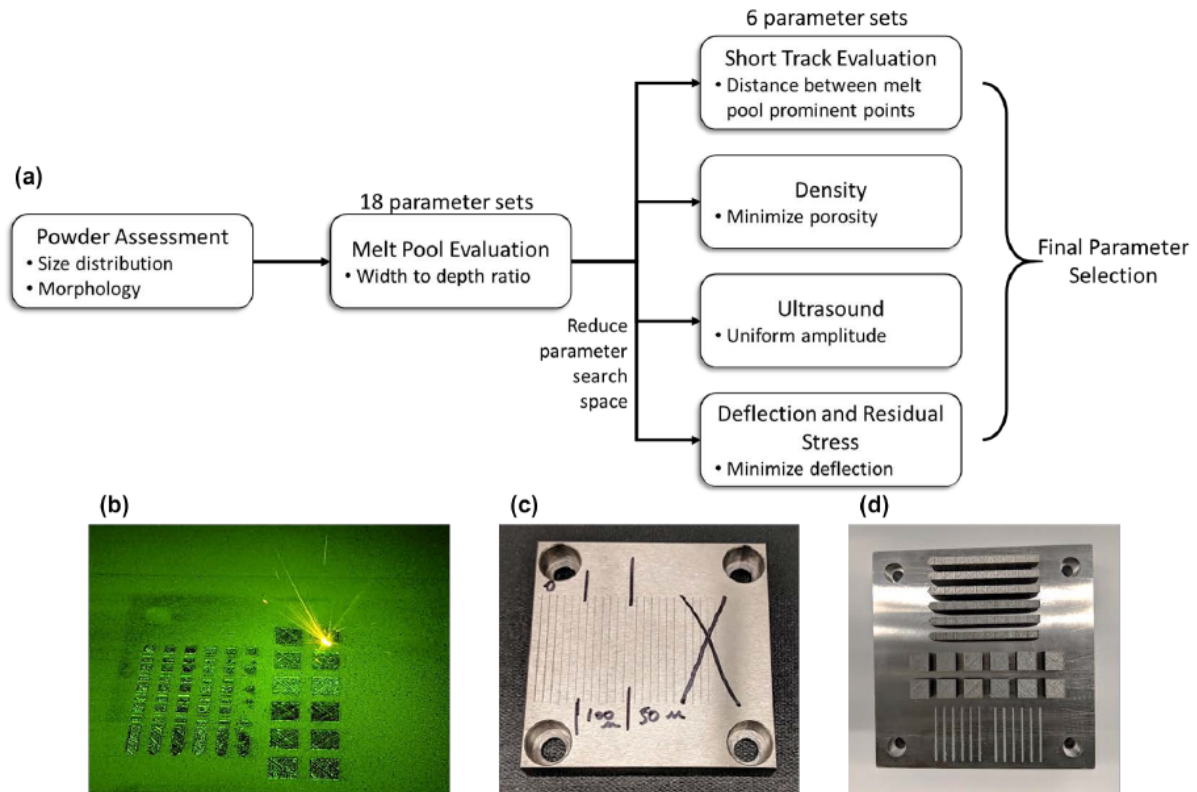
Figure 1. (a) Process parameter selection framework. (b) Image captured during the laser powder bed fusion process. (c) Melt pool evaluation build plate. (d) Development build plate.

Powder Feedstock Assessment

A high-carbon steel powder (8620; Sandvik Osprey, Sweden) was selected as the raw material for the AM rollers given its availability in the desired nominal particle size distribution, hardenability, and composition similarity to other bearing steel alloys. Before powder feedstock was loaded into the LPBF system, it was necessary to ensure that it met the system morphology and size distribution requirements. For this purpose, images of the powder were acquired using a Helios NanoLab 660 scanning electron microscope (SEM) and post-processed using open source image processing software [51]. An example SEM image is shown in Fig. 2(a), where it can be observed the particles are mostly spherical. The presence of satellite particles and some rough particle surfaces is noted; however, the powder morphology was deemed satisfactory for the LPBF system (Lumex Avance-25). The SEM images were thresholded to isolate individual powder particles, and the particle diameters were quantified assuming a spherical morphology. A total of 2417 particles from 10 images were quantified and the resulting histogram is shown in Fig. 2(b). As noted in the histogram, the mean particle size was 47.0 ± 16.9 μm (D10, D50, D90 of 27.5, 46.6, and 67.0 μm respectively). Thus, the powder was determined to be acceptable for AM processing.
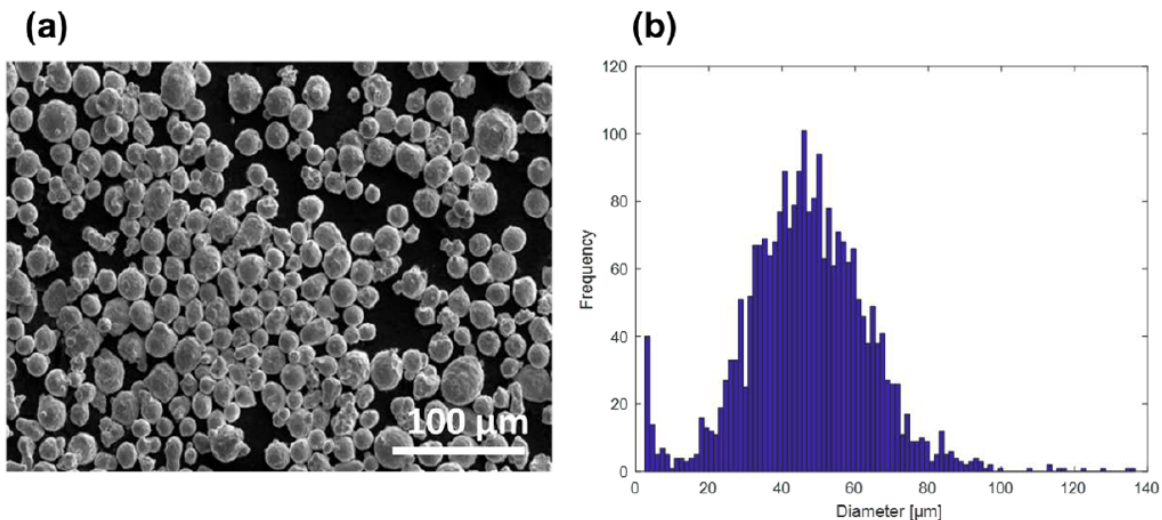

Figure 2. (a) SEM image (scale bar = 100 μm), (b) powder diameter distribution

Melt Pool Evaluation

A total of 18 parameter sets were defined for initial melt pool evaluation by varying the layer thickness, t, and the laser power, P, while maintaining a laser scanning speed, s, of 700 mm/s and spot size, a, of 200 µm. To study the melt pool, layer thicknesses of 0, 50, and 100 µm were used, where the sets with 0 µm layer thickness served as a baseline for comparison. Similarly, laser powers of 160, 180, 250, 320, 390, and 460 W were used. Note that by changing the laser power the linear energy density input $E_L = P/s$ [52] also changed.

A single line track was printed for each of the 18 parameter combinations as pictured in Fig. 1(c), the tracks were visually inspected for continuity, and the build plate was cut in the direction perpendicular to the tracks at approximately one third of the track length such that the melt pools were exposed. Then the cross-section of the melt pools was prepared for metallography, and the optical images of the melt pools were captured using a Keyence laser scanning confocal microscope (LSCM). The melt pool images were used to quantify the average melt pool width and depth corresponding to each parameter combination as defined in Fig. 3(a). A desirable melt pool width-to-depth ratio is $W/D > 1.5$ [43], lower ratios are associated with keyhole-type melt pools and instabilities. Additionally, it is important that the melt pool depth is greater than the desired layer thickness to avoid lack of fusion interlayer defects. A parameter map along with the obtained W/D ratios is given in Fig. 3(b), along with example images of unacceptable and acceptable melt pools indicated with red and green arrows respectively. Based on the results of this evaluation, 6 parameter sets were considered for volumetric measurements, namely layer thickness of 50, and 100 µm and laser power of 250, 320, and 390 W.
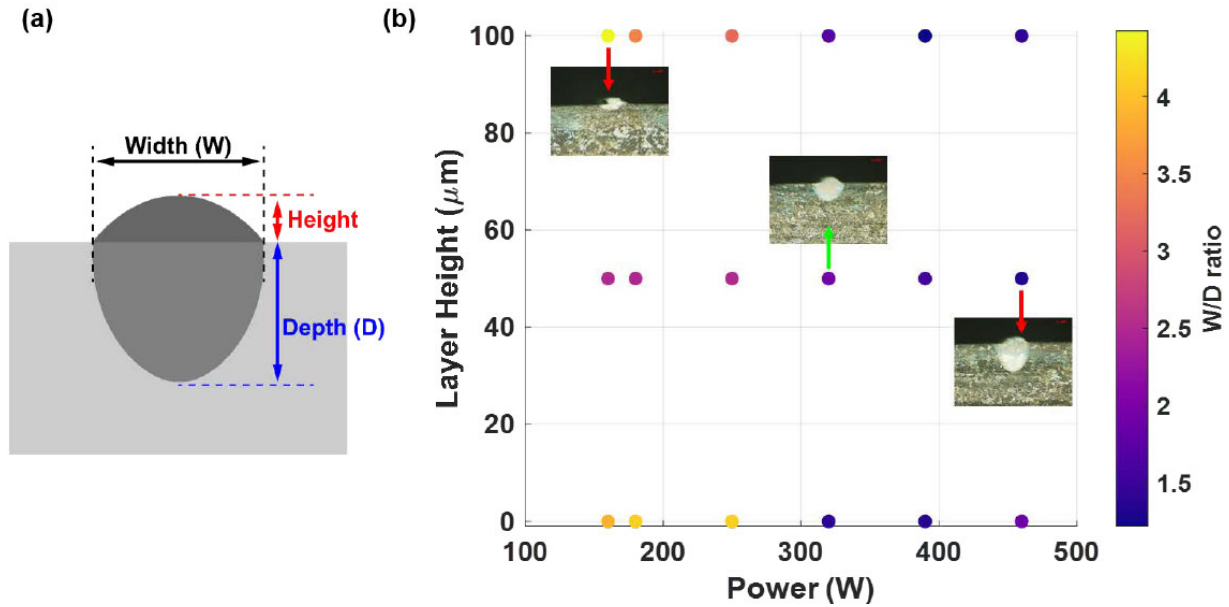
Figure 3. Melt pool evaluation parameters and corresponding width, W, to depth, D, ratio results. Example images of unacceptable and acceptable melt pools are shown with red and green arrows respectively.

Short Track Evaluation

A series of short tracks were manufactured to study inter and intra layer bonding and geometry uniformity. The short tracks were 5 single tracks wide, 4 layers high and 30 mm long. For each parameter combination, two tracks were built as seen in the bottom of the build plate on Fig. 1(d), for a total of 12 tracks. The tracks were then cut approximately in half in the direction perpendicular to their length to expose their cross-section. The cross-section was then prepared metallographically and imaged with LSCM. The images obtained were visually inspected and no inter- or intra-layer cracking was observed. Furthermore, varying measures were quantified including the horizontal and vertical distances between melt pool valleys. In all cases the horizontal distances were greater than the hatch spacing which ensures full densification. Then the ratio of the vertical distances to the nominal layer height was defined as the measured depth/layer height ratio. As this ratio increases, the possibility of interlayer porosity decreases. A map of the process

parameters and resulting depth/layer height latter ratio is shown in Fig. 4 with representative

images of acceptable and unacceptable track cross-sections in green and red arrows respectively.
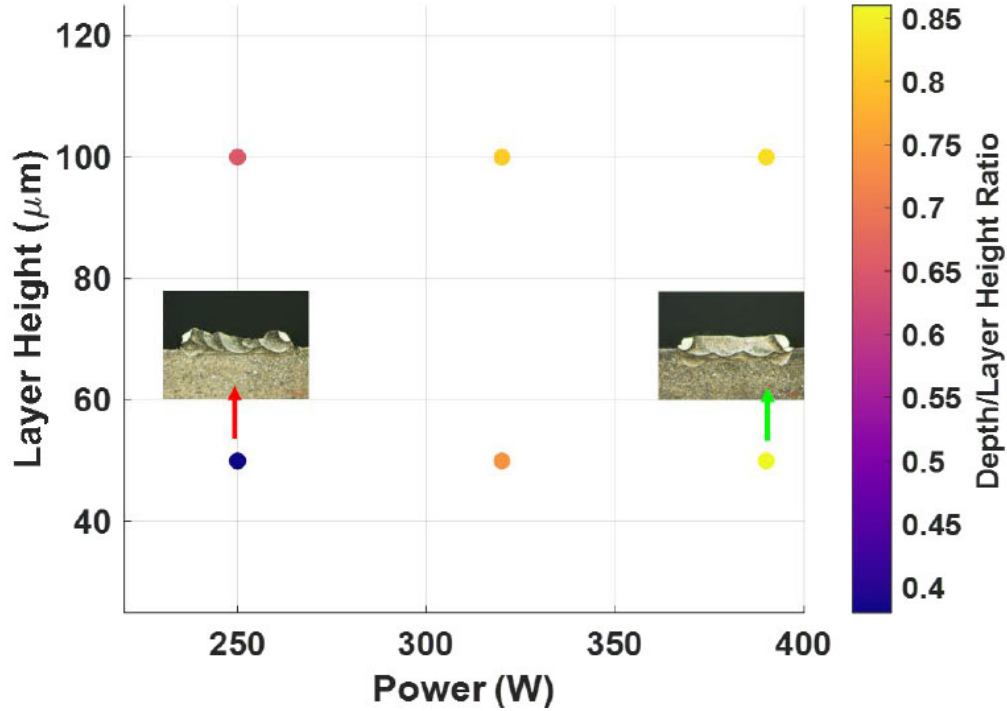

Figure 4. Short track evaluation parameters and corresponding depth to layer height ratio results. Example images of acceptable and unacceptable short tracks are shown with green and red arrows respectively.

Density

The next set of assessments were based on 10 x 10 x 10 mm^3 cubes that were manufactured for

volumetric uniformity. Two cubes were made for each of the process parameters sets for a total of

12 cubes as listed in Table 1. Because the porosity in the samples was low and there were no

exposed pores, the Archimedes method was used to quantify each sample density [53] with respect

to the nominal 8620 steel density of 7.85 g/cm^3. To measure the density of a sample with this

approach, the mass of the sample in air m_a and in water m_f were measured, then the sample

density ρ_s was obtained using

$$\rho_s = \frac{m_a}{m_a - m_f}\left(\rho_f - \rho_a\right) + \rho_a,$$

where $\rho_f = 0.9982$ g/cm^3 is the density of water and $\rho_a = 0.0012$ g/cm^3 is the density of air. The measurements were obtained with a precision balance equipped with an Archimedes setup (Mettler Toledo AT201). The results show that the density of most cubes was > 99.5%, although one pair (samples 7 and 8) had significantly lower density.

Table 1. Archimedes density measurement results.

Sample	Power (W)	Layer Height (µm)	Density (g/cm^3)	Density %
1	250	50	7.824	99.66
2	250	50	7.834	99.79
3	320	50	7.824	99.67
4	320	50	7.83	99.74
5	390	50	7.807	99.45
6	390	50	7.813	99.53
7	250	100	7.326	**93.33**
8	250	100	7.339	**93.50**
9	320	100	7.748	98.71
10	320	100	7.732	98.49
11	390	100	7.783	99.15
12	390	100	7.776	99.06

Ultrasonic Assessment of Microstructure

The 12 cubes were also scanned using normal incidence ultrasound with spherically focused transducers (Olympus) at 7.5, 10, and 15 MHz and in a pulse-echo immersion setup [54]. Given the low porosity, any large differences in scattering amplitude were mainly attributed to microstructure heterogeneity [55]. An example scan showing the spatial distribution of scattering amplitude with respect to the sample geometry is provided in Fig. 5(a). To quantify the scattering from each sample, the spatial variance of the measured amplitude was averaged over a time window equivalent to the nominal transducer pulse width for each frequency and normalized by the maximum possible voltage for each measurement [54]. This quantity is equivalent to the energy

scattered back to the transducer from the sample microstructure near the depth of the transducer focus (~5 mm). A larger amount of backscattered energy is indicative of higher heterogeneity within the microstructure. The resulting backscattered energy at each measured frequency is shown for each sample in Fig. 5(b).
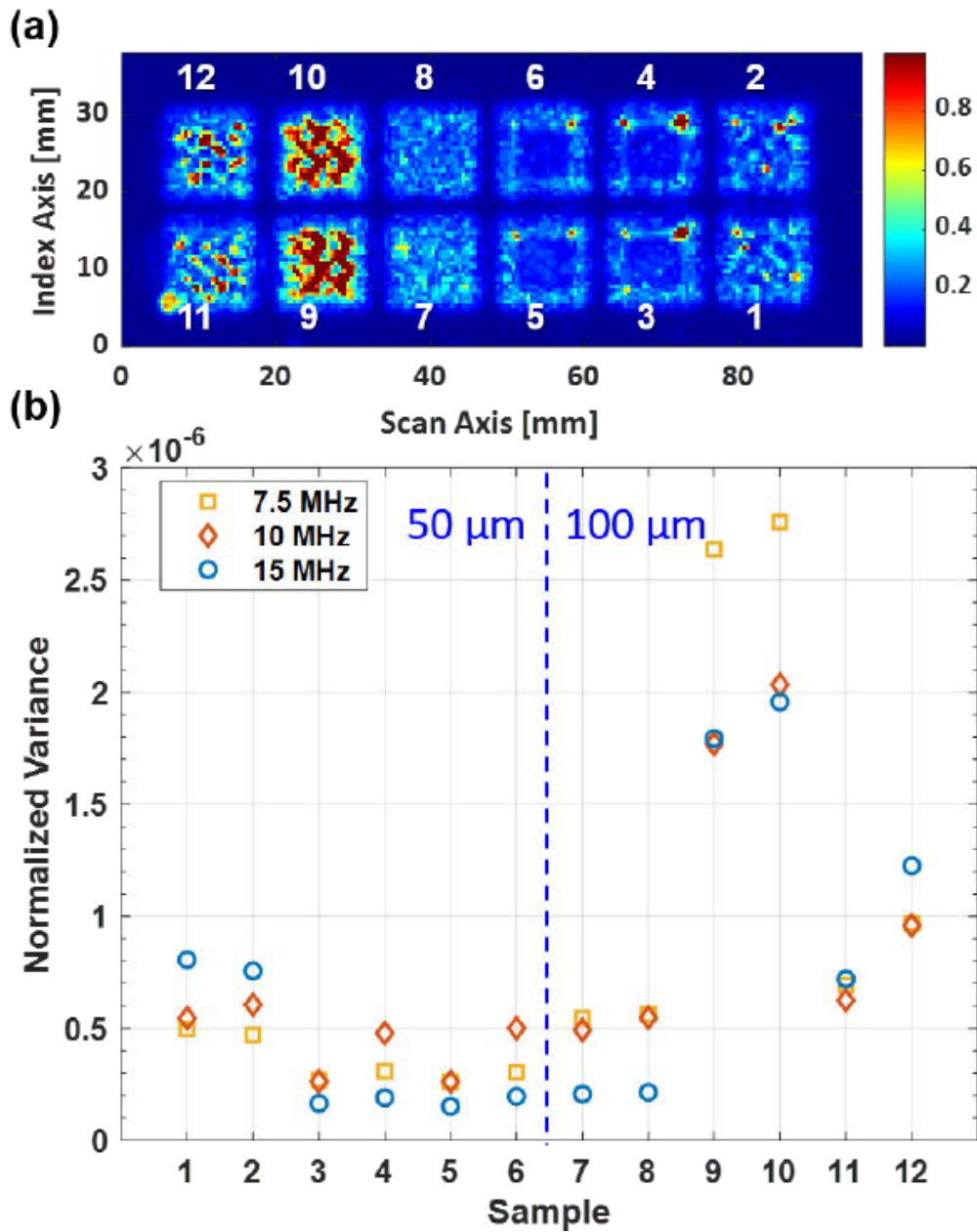

Figure 5. (a) Example 10 MHz amplitude C-scan, (b) Normalized backscattered ultrasonic energy for all samples.

Deflection and Residual Stress

The NIST bridge geometry for benchmark testing described in [50] was used to evaluate the residual stress associated with each process parameter combination. A bridge was made for each of the process parameter combinations for a total of six bridges. While the bridges were still on the build plate, a wire EDM cut was made across the bottom of each bridge as close to the build plate as possible stopping right before the thickest portion of the bridge as shown in red in Fig. 6(a). Then a point cloud three-dimensional scanner was used to collect measurements of the vertical height along the length of each bridge z_f with respect to the build plate height z_o. The total deflection was then calculated as $\delta = z_f - z_o$. Thus, a qualitative residual stress evaluation was obtained based on the measured bridge deflection as seen in Fig. 6(b), where positive deflection was indicative of tensile residual stresses.
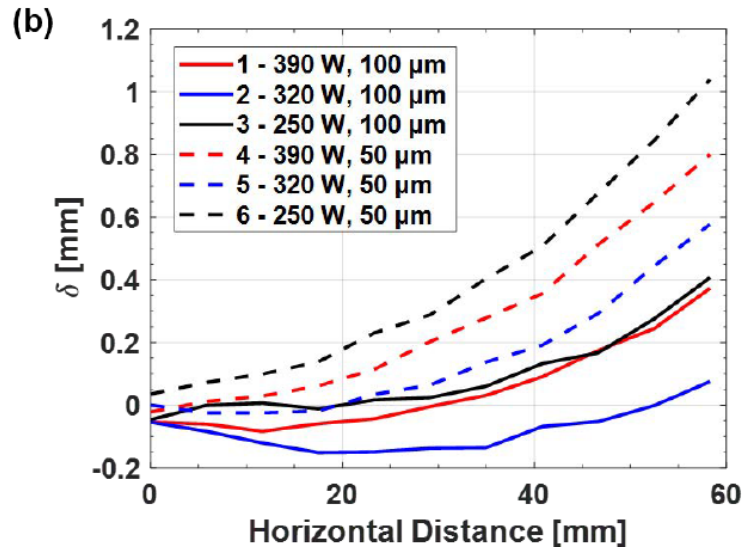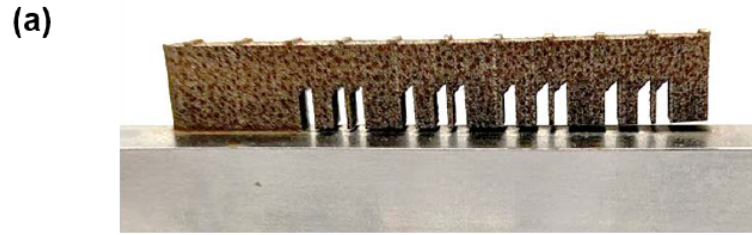
Figure 6. NIST bridge deflection measurements. (a) Image of a bridge showing deflection after cut due to residual stress. (b) Deflection measurement results for all samples, where higher deflection indicates higher tensile residual stresses.

Final Parameter Selection

Finally, the results obtained from each of the volumetric measurements were evaluated for each process parameter in a decision matrix as shown in Table 2. For each measurement, the parameters were ranked 1 through 6, with 6 being the most desirable. Additionally, the density and residual stress measurements had double the weight because they had been originally defined as the most important characteristics based on the application. The totals from the decision matrix resulted in a laser power of 320 W with a layer height of 50 μm.

Table 2. Decision matrix for final parameter selection.

Test	Laser power and layer height					
	250 W 50 µm	320 W 50 µm	390 W 50 µm	250 W 100 µm	320 W 100 µm	390 W 100 µm
Tracks	2	4	6	1	3	5
Density	6	5	4	1	2	3
Ultrasound	6	4	5	3	1	2
Deflection	1	3	2	4	6	5
Totals	**22**	**24**	**23**	**14**	**20**	**23**

MANUFACTURING AND POST-PROCESSING

Based on the build parameters defined above (320 W laser power; 50 µm layer thickness), fifty

rollers were manufactured with LPBF in order to have 46 for a Class K double-row tapered roller

bearing (152.4 mm x 228.6 mm), with extra rollers in case of localized print failure. Other

parameters included a hatch spacing of 120 µm, scan direction of 45°, randomized scanning order,

and cell size of 5 mm x 5 mm. The rollers were slightly oversized with a height of 50.18 mm and

with a linear taper from a major diameter of 22.69 mm to a minor diameter of 21.01 mm. An

additional 3 mm were included at the bottom of each roller to account for removal from the build

plate. In addition, two rectangular bars for tensile testing were included in the build. The bars were

oriented in two orthogonal directions to uncover any potential directional dependence. The planned

print layout and a photograph of the final build are shown in Fig. 7. It should be noted that one of

the rectangular bars and a few nearby rollers cracked early in the build (~9 mm from the top of the

build plate; no further cracking was observed). The affected rollers were not used in subsequent

tests. After manufacturing, the entire build plate with all components was heated in a furnace to

205 °C and held at that temperature for 1 hour to relieve residual stresses. Afterwards, the rollers

and components for tensile bars were removed from the build plate. The rollers were machined

and carburized to the design specifications to match the CM rollers that were made from 8720M

bearing quality steel. Each rectangular bar was machined into two tensile bars for mechanical

testing. As shown in Table 3, the properties of the material were sufficient for the purpose here. In addition, Rockwell hardness (HRC) and effective case depth (ECD) were assessed for each group of rollers. As shown in Table 4 the properties of each set of rollers are comparable.
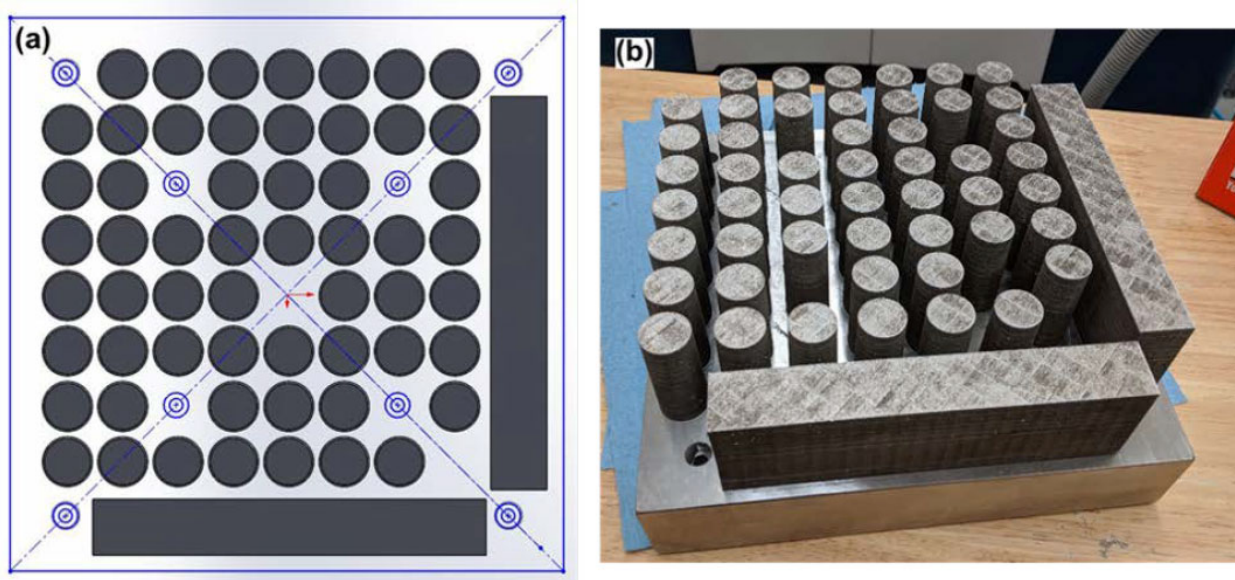

Figure 7. (a) Top view of the design layout for the additive manufacturing of the rollers and tensile bars. (b) Photograph of the final parts on the build plate.

Table 3. Results of mechanical tests of the metal AM test bars.

Sample ID	Original area (cm²)	Reduction of area (%)	Yield Strength (GPa)	Tensile Strength (GPa)	Elongation using 50.8 mm gage length (%)
X, top	1.29	1.2	1.26	1.39	10.0
X, bottom	1.29	1.6	1.26	1.41	10.0
Y, top	1.28	18.5	1.27	1.44	7.0
Y, bottom	0.330	32.2	1.31	1.38	12.0*

*Based on a 25.4 mm gage length

Table 4. Rockwell hardness (HRC) and effective case depth (average and standard deviation) for the AM and CM rollers.

	Core hardness (HRC)		Surface hardness (HRC)		Effective case depth (mm)	
Roller type	AVG	STD	AVG	STD	AVG	STD
AM	43.2	2.97	59.1	1.75	2.13	0.533
CM	36.4	1.58	60.3	1.36	1.75	0.203

FATIGUE LIFE TESTING

Two different tests were performed to compare the AM rollers to CM rollers. Both tests used rollers within a Class K bearing. The first, was an accelerated life test, in which 12 AM rollers were assembled into two inner ring assemblies (6 rollers each) along with 34 CM rollers (17 rollers each) to complete the inner ring/roller assemblies. These assemblies were installed into a bearing outer ring and placed in the test rig. The test began with the rig set to 300 rpm and an axial load of 3.93 kN. During the test, load and speed were increased. The bearing failed after approximately 28 days. The event log for this test is shown in Table 5.

Table 5. Accelerated life test event log. The speed of the test and the axial load are both shown.

Day	Action/Observation
0	Test start: 300 rpm; 3.93 kN
0	Load increased to 15.7 kN
5	Speed increased to 500 rpm
7	Load increased to 23.6 kN
11	Load increased to 31.4 kN
12	Load increased to 39.3 kN
15	Load increased to 47.2 kN
15	Load increased to 62.9 kN
15	Temperature increased too much; load reduced to 55.0 kN
27	Rig automatically stopped; bearing failure

The inner ring/roller assemblies were removed from the bearing and all components were visually inspected. The inboard (IB) cage was disintegrated with no cage bars remaining. Fig. 8(a) shows the IB inner ring/roller assembly inside of the bearing, and Fig. 8(b) shows the same assembly after removal from the bearing. The IB inner ring showed evidence of spalling toward the small end of the raceway as shown in Fig. 9. The outboard (OB) inner ring showed no sign of defects other than fragment indentations. The IB outer ring raceway possessed fragment indentations, heat and smearing. The OB outer ring raceway, like the inner ring, showed no sign of defects other than small amounts of fragment indentations. Fig. 10(a) and Fig. 10(b) compare the IB and OB outer ring raceways, respectively. The IB rollers, both AM and CM, all had evidence of spalling toward the small end of the raceways, as shown in Fig. 11(a) and Fig. 11(b). All IB rollers showed a similar degree of damage.

Figure 8. Results from the accelerated life test: (a) IB inner ring assembly, (b) IB inner ring assembly removed from the bearing

Figure 9. Results from the accelerated life test: IB and OB inner ring raceways.

Figure 10. Results from the accelerated life test: (a) IB outer ring raceway, (b) OB outer ring raceway
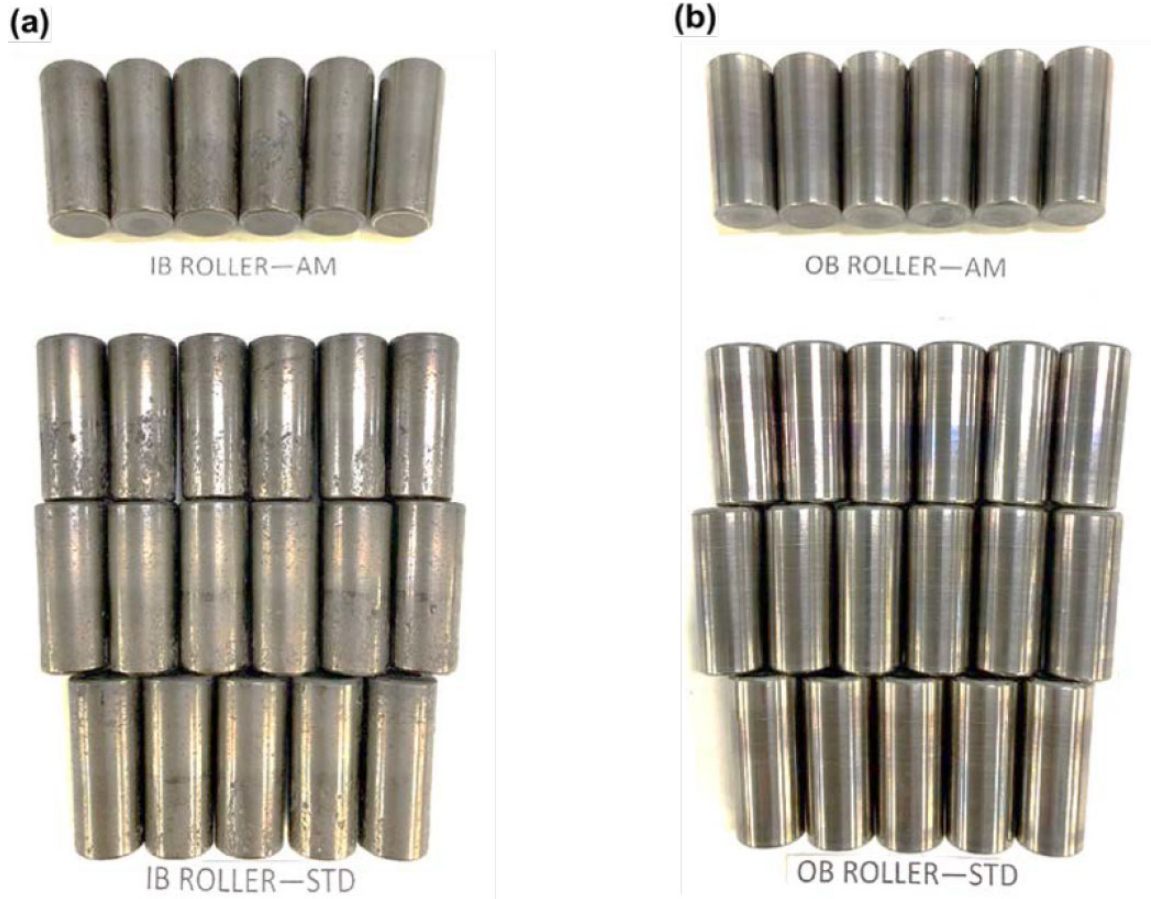
*Figure 11. Results from the accelerated life test: (a) IB rollers, (b) OB rollers*

SIMULATED SERVICE LIFE TESTING

For the second fatigue test, rollers were assembled into Association of American Railroads (AAR) Class K bearings for fatigue testing. Twenty-three (23) AM rollers were assembled into the inboard (IB) cone assembly of bearing 7342 and twenty-three (23) CM rollers were assembled into the outboard (OB) cone assembly of bearing 6867. These two positions were chosen because they experience the same load conditions on the test rig. See Fig. 12 for the test layout. The bearings were subjected to a load of 110% of AAR loading (168.4 kN) and run for 252,940 simulated miles.
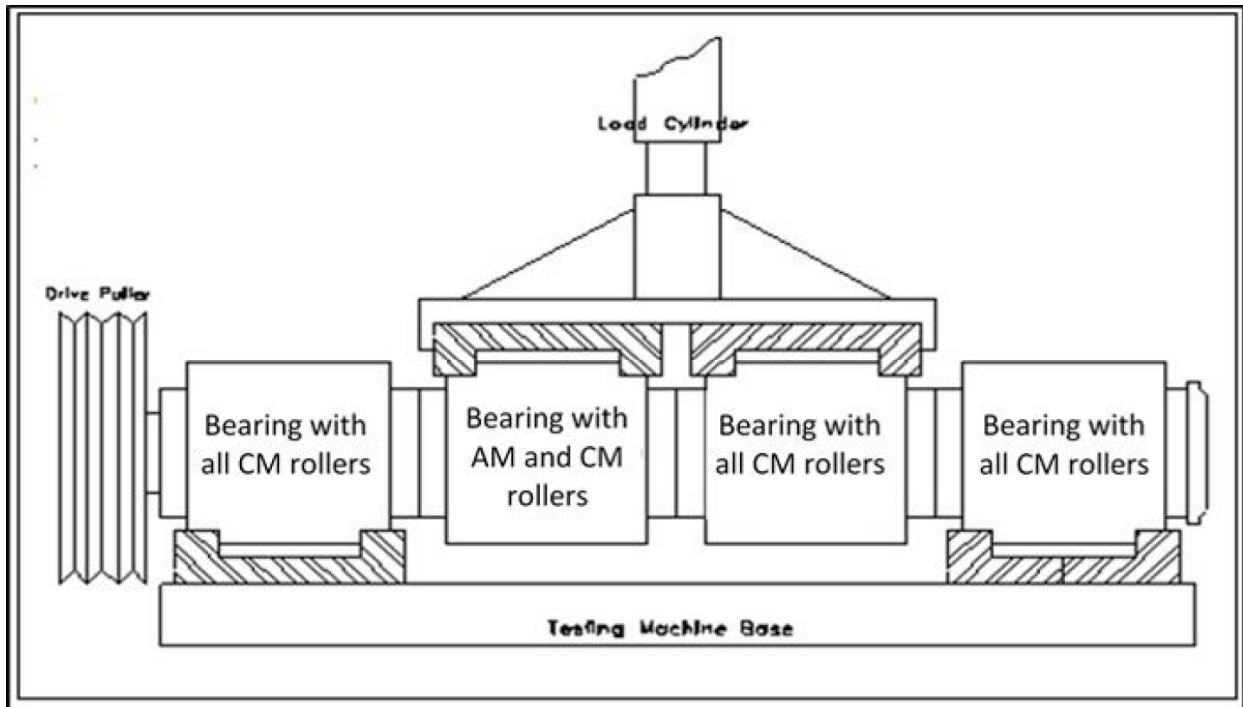
Figure 12. Schematic of the simulated service life test rig with all bearing positions indicated. The AM rollers were in the inner ring beneath the load cylinder.

At the conclusion of the test, the bearings were dismounted from the axle, disassembled, and the cages removed from the test inner ring assemblies. Visual inspection showed no detrimental conditions on any test components as shown in Fig. 13-15. Based on this visual inspection, the AM rollers performed as well as the CM rollers.
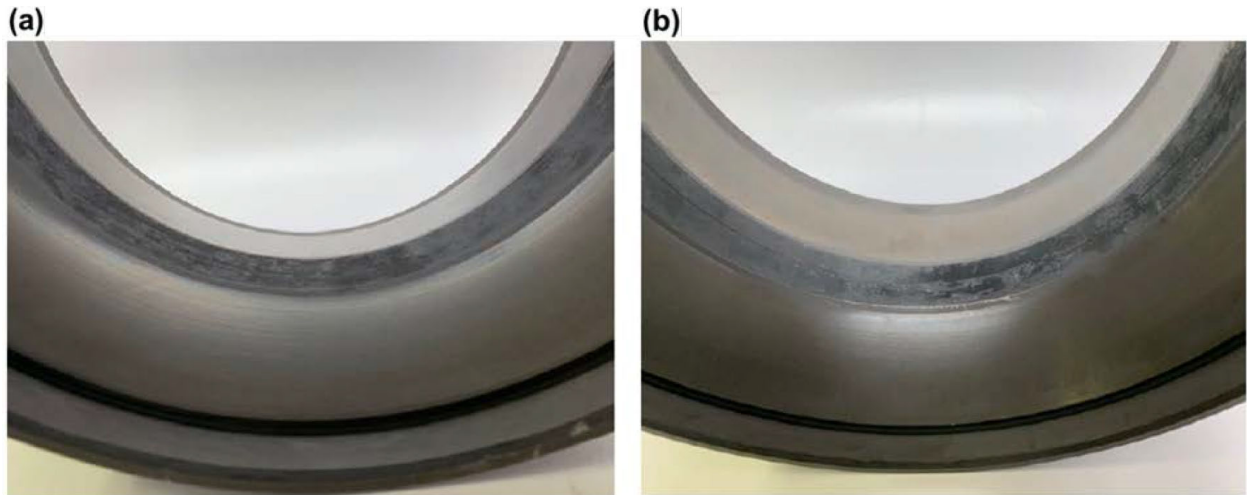
Figure 13. Photographs of the outer ring raceways at the conclusion of the simulated service life test: (a) bearing 6876 OB outer ring raceway (CM rollers), (b) bearing 7342 IB outer ring raceway (AM rollers).
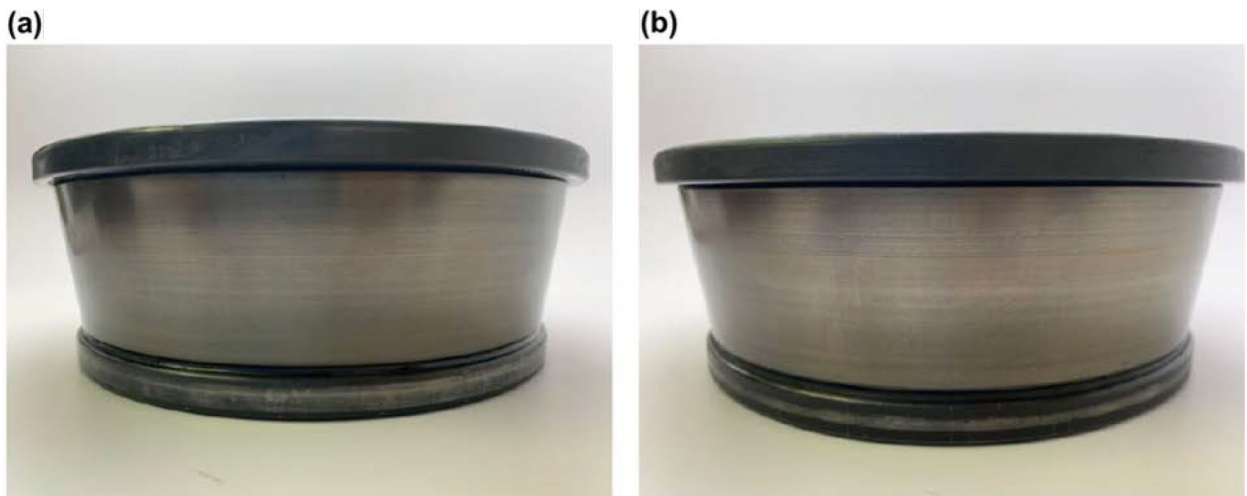
Figure 14. Photographs of the inner ring raceways at the conclusion of the simulated service life test: (a) bearing 6876 OB inner ring (CM rollers), (b) bearing 7342 IB inner ring raceway (AM rollers).
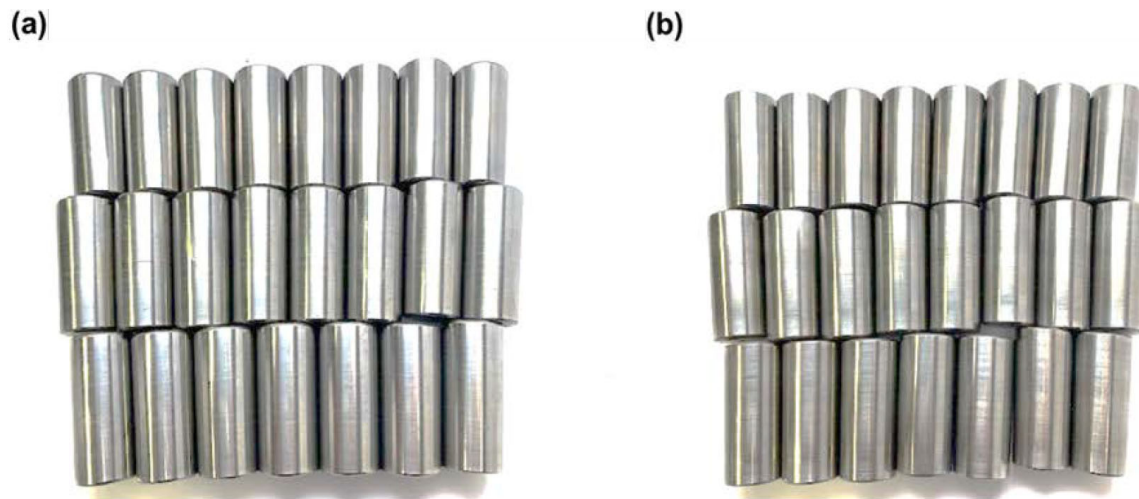
Figure 15. Photographs of the rollers at the conclusion of the simulated service life test: (a) CM rollers, (b) AM rollers.

DISCUSSION

In this article, railroad bearing rollers were created using metal additive manufacturing (AM) and the rollers were integrated within tapered roller bearings in order to evaluate their performance with respect to rolling contact fatigue (RCF). The AM rollers were studied using conventionally manufactured (CM) rollers as the metric for comparison. The AM process parameter development highlighted the variations that can occur for critical material conditions based on the AM inputs. Parameters such as the laser power, layer thickness, and laser scan speed affected the component porosity, microstructure, and residual stresses all of which influence RCF. The range of parameters examined led to an adequate choice for component manufacturing, but it may not have been the optimal choice.

Despite these challenges, the AM roller performance was comparable to that of the CM rollers for both an accelerated life test and a simulated service life test. Although the results at this stage may be considered to be qualitative, they are certainly encouraging. The severity of the accelerated life

test resulted in large spalls on all rollers, but the condition of the AM rollers was similar to that of the CM rollers. In addition, no damage was visible on the AM rollers (nor the CM rollers) after more than 250,000 miles of simulated service life. A much longer test (e.g., one-million miles) may be needed to capture any differences between these manufacturing approaches. However, it is clear that new component designs can be pursued to take advantage of the full impact that AM has to offer.

CONCLUSIONS

Metal AM is making major impacts within the aerospace and biomedical industries because of the new design opportunities that can be exploited with this exciting approach. Currently, the cost of AM is still not at a point of viability for the railroad industry, but efficiencies with metal AM will continue to improve such that it may soon prove to be of value for certain situations for railroads and OEMs.

There is also a large amount of future work needed to understand more fully the material state of the AM rollers. The porosity, especially with respect to the pore size distribution, the pore spatial organization, and the pore shapes should be quantified and the presence of impurities evaluated. The microstructure and hardness profile near the surface will also provide insights into their performance which was surprisingly good.

ACKNOWLEDGEMENTS

REFERENCES

[1] C. Tarawneh, J. Montalvo, and B. Wilson, "Defect detection in freight railcar tapered-roller bearings using vibration techniques," *Rail. Eng. Science*, vol. 29, no. 1, pp. 42–58, Mar. 2021, doi: 10.1007/s40534-020-00230-x.

[2] F. Sadeghi, B. Jalalahmadi, T. S. Slack, N. Raje, and N. K. Arakere, "A Review of Rolling Contact Fatigue," *Journal of Tribology*, vol. 131, no. 4, Sep. 2009, doi: 10.1115/1.3209132.

[3] T. A. Harris and M. N. Kotzalas, *Advanced Concepts of Bearing Technology: Rolling Bearing Analysis, Fifth Edition*, 5th ed. Boca Raton: CRC Press, 2006. doi: 10.1201/9781420006582.

[4] M. A. Mason, C. P. Cartin, P. Shahidi, M. W. Fetty, and B. M. Wilson, "Hertzian Contact Stress Modeling in Railway Bearings for Assorted Load Conditions and Geometries," *Proceedings of the 2014 Joint Rail Conference*, Jun. 2014. doi: 10.1115/JRC2014-3846.

[5] C. J. Hassila, P. Harlin, and U. Wiklund, "Rolling contact fatigue crack propagation relative to anisotropies in additive manufactured Inconel 625," *Wear*, vol. 426–427, pp. 1837–1845, Apr. 2019, doi: 10.1016/j.wear.2019.01.085.

[6] Z. Liu, Z. Wang, C. Gao, X. Liu, R. Liu, Z. Xiao, and J. Sanderson, "Enhanced rolling contact fatigue behavior of selective electron beam melted Ti6Al4V using the ultrasonic surface rolling process," *Materials Science and Engineering: A*, vol. 833, p. 142352, Jan. 2022, doi: 10.1016/j.msea.2021.142352.

[7] J. Yang, W. Ma, W. Zhang, X. Wang, K. Huang, Z. Liu, Z. Zhou, H. Xu, and J. Xiao, "The dynamic load-bearing performance of the laser cladding Fe-based alloy on the U75V rail," *International Journal of Fatigue*, vol. 165, p. 107180, Dec. 2022, doi: 10.1016/j.ijfatigue.2022.107180.

[8] A. Vafadar, F. Guzzomi, A. Rassau, and K. Hayward, "Advances in Metal Additive Manufacturing: A Review of Common Processes, Industrial Applications, and Current Challenges," *Applied Sciences*, vol. 11, no. 3, Art. no. 3, Jan. 2021, doi: 10.3390/app11031213.

[9] M. Dilberoglu, B. Gharehpapagh, U. Yaman, and M. Dolen, "Current trends and research opportunities in hybrid additive manufacturing," *Int J Adv Manuf Technol*, vol. 113, no. 3, pp. 623–648, Mar. 2021, doi: 10.1007/s00170-021-06688-1.

[10] J. C. Najmon, S. Raeisi, and A. Tovar, "2 - Review of additive manufacturing technologies and applications in the aerospace industry," in *Additive Manufacturing for the Aerospace Industry*, F. Froes and R. Boyer, Eds. Elsevier, 2019, pp. 7–31. doi: 10.1016/B978-0-12-814062-8.00002-9.

[11] D. Greitemeier, F. Palm, F. Syassen, and T. Melz, "Fatigue performance of additive manufactured TiAl6V4 using electron and laser beam melting," *International Journal of Fatigue*, vol. 94, pp. 211–217, Jan. 2017, doi: 10.1016/j.ijfatigue.2016.05.001.

[12] N. Sanaei and A. Fatemi, "Defects in additive manufactured metals and their effect on fatigue performance: A state-of-the-art review," *Progress in Materials Science*, vol. 117, p. 100724, Apr. 2021, doi: 10.1016/j.pmatsci.2020.100724.

[13] T. M. Mower and M. J. Long, "Mechanical behavior of additive manufactured, powder-bed laser-fused materials," *Materials Science and Engineering: A*, vol. 651, pp. 198–213, Jan. 2016, doi: 10.1016/j.msea.2015.10.068.

[14] K. S. Chan, M. Koike, R. L. Mason, and T. Okabe, "Fatigue Life of Titanium Alloys Fabricated by Additive Layer Manufacturing Techniques for Dental Implants," *Metall Mater Trans A*, vol. 44, no. 2, pp. 1010–1022, Feb. 2013, doi: 10.1007/s11661-012-1470-4.

[15] E. Wycisk, S. Siddique, D. Herzog, F. Walther, and C. Emmelmann, "Fatigue Performance of Laser Additive Manufactured Ti–6Al–4V in Very High Cycle Fatigue Regime up to 109 Cycles," *Frontiers in Materials*, vol. 2, 2015.

[16] G. Kasperovich and J. Hausmann, "Improvement of fatigue resistance and ductility of TiAl6V4 processed by selective laser melting," *Journal of Materials Processing Technology*, vol. 220, pp. 202–214, Jun. 2015, doi: 10.1016/j.jmatprotec.2015.01.025

[17] N. Hrabe, T. Gnäupel-Herold, and T. Quinn, "Fatigue properties of a titanium alloy (Ti–6Al–4V) fabricated via electron beam melting (EBM): Effects of internal defects and residual stress," *International Journal of Fatigue*, vol. 94, pp. 202–210, Jan. 2017, doi: 10.1016/j.ijfatigue.2016.04.022.

[18] L. Carneiro, B. Jalalahmadi, A. Ashtekar, and Y. Jiang, "Cyclic deformation and fatigue behavior of additively manufactured 17–4 PH stainless steel," *International Journal of Fatigue*, vol. 123, pp. 22–30, Jun. 2019, doi: 10.1016/j.ijfatigue.2019.02.006.

[19] H. K. Rafi, T. L. Starr, and B. E. Stucker, "A comparison of the tensile, fatigue, and fracture behavior of Ti–6Al–4V and 15-5 PH stainless steel parts made by selective laser melting," *Int J Adv Manuf Technol*, vol. 69, no. 5, pp. 1299–1309, Nov. 2013, doi: 10.1007/s00170-013-5106-7.

[20] A. Fatemi, R. Molaei, S. Sharifimehr, N. Shamsaei, and N. Phan, "Torsional fatigue behavior of wrought and additive manufactured Ti-6Al-4V by powder bed fusion including surface finish effect," *International Journal of Fatigue*, vol. 99, pp. 187–201, Jun. 2017, doi: 10.1016/j.ijfatigue.2017.03.002.

[21] D. B. Witkin, D. Patel, T. V. Albright, G. E. Bean, and T. McLouth, "Influence of surface conditions and specimen orientation on high cycle fatigue properties of Inconel 718 prepared by

laser powder bed fusion," *International Journal of Fatigue*, vol. 132, p. 105392, Mar. 2020, doi: 10.1016/j.ijfatigue.2019.105392.

[22] G. Nicoletto, "Influence Of Rough As-Built Surfaces On Smooth and Notched Fatigue Behavior of L-PBF Alsi10mg," *Additive Manufacturing*, vol. 34, p. 101251, Aug. 2020, doi: 10.1016/j.addma.2020.101251.

[23] P. Edwards and M. Ramulu, "Fatigue performance evaluation of selective laser melted Ti–6Al–4V," *Materials Science and Engineering: A*, vol. 598, pp. 327–337, Mar. 2014, doi: 10.1016/j.msea.2014.01.041.

[24] N. Kalentics, M. O. V. de Seijas, S. Griffiths, C. Leinenbach, and R. E. Logé, "3D laser shock peening – A new method for improving fatigue properties of selective laser melted parts," *Additive Manufacturing*, vol. 33, p. 101112, May 2020, doi: 10.1016/j.addma.2020.101112.

[25] J. Günther *et al.*, "Fatigue life of additively manufactured Ti–6Al–4V in the very high cycle fatigue regime," *International Journal of Fatigue*, vol. 94, pp. 236–245, Jan. 2017, doi: 10.1016/j.ijfatigue.2016.05.018.

[26] R. Molaei *et al.*, "Fatigue of additive manufactured Ti-6Al-4V, Part II: The relationship between microstructure, material cyclic properties, and component performance," *International Journal of Fatigue*, vol. 132, p. 105363, Mar. 2020, doi: 10.1016/j.ijfatigue.2019.105363.

[27] V. Chastand, A. Tezenas, Y. Cadoret, P. Quaegebeur, W. Maia, and E. Charkaluk, "Fatigue characterization of Titanium Ti-6Al-4V samples produced by Additive Manufacturing," *Procedia Structural Integrity*, vol. 2, pp. 3168–3176, Jan. 2016, doi: 10.1016/j.prostr.2016.06.395.

[28] A. Fatemi, R. Molaei, S. Sharifimehr, N. Phan, and N. Shamsaei, "Multiaxial fatigue behavior of wrought and additive manufactured Ti-6Al-4V including surface finish effect,"

International Journal of Fatigue, vol. 100, pp. 347–366, Jul. 2017, doi:

10.1016/j.ijfatigue.2017.03.044.

[29] P. Li, D. H. Warner, J. W. Pegues, M. D. Roach, N. Shamsaei, and N. Phan, "Towards

predicting differences in fatigue performance of laser powder bed fused Ti-6Al-4V coupons from

the same build," *International Journal of Fatigue*, vol. 126, pp. 284–296, Sep. 2019, doi:

10.1016/j.ijfatigue.2019.05.004.

[30] S. Romano, P. D. Nezhadfar, N. Shamsaei, M. Seifi, and S. Beretta, "High cycle fatigue

behavior and life prediction for additively manufactured 17-4 PH stainless steel: Effect of sub-

surface porosity and surface roughness," *Theoretical and Applied Fracture Mechanics*, vol. 106,

p. 102477, Apr. 2020, doi: 10.1016/j.tafmec.2020.102477.

[31] K. Solberg and F. Berto, "The effect of defects and notches in quasi-static and fatigue

loading of Inconel 718 specimens produced by selective laser melting," *International Journal of

Fatigue*, vol. 137, p. 105637, Aug. 2020, doi: 10.1016/j.ijfatigue.2020.105637.

[32] H. Zhang, D. Dong, S. Su, and A. Chen, "Experimental study of effect of post processing on

fracture toughness and fatigue crack growth performance of selective laser melting Ti-6Al-4V,"

Chinese Journal of Aeronautics, vol. 32, no. 10, pp. 2383–2393, Oct. 2019, doi:

10.1016/j.cja.2018.12.007.

[33] S. Leuders *et al.*, "On the mechanical behaviour of titanium alloy TiAl6V4 manufactured by

selective laser melting: Fatigue resistance and crack growth performance," *International Journal

of Fatigue*, vol. 48, pp. 300–307, Mar. 2013, doi: 10.1016/j.ijfatigue.2012.11.011.

[34] S. Tammas-Williams, P. J. Withers, I. Todd, and P. B. Prangnell, "The Influence of Porosity

on Fatigue Crack Initiation in Additively Manufactured Titanium Components," *Sci Rep*, vol. 7,

no. 1, Art. no. 1, Aug. 2017, doi: 10.1038/s41598-017-06504-5.

[35] J. W. Pegues, M. D. Roach, and N. Shamsaei, "Effects of Postprocess Thermal Treatments on Static and Cyclic Deformation Behavior of Additively Manufactured Austenitic Stainless Steel," *JOM*, vol. 72, no. 3, pp. 1355–1365, Mar. 2020, doi: 10.1007/s11837-019-03983-x.

[36] R. Molaei, A. Fatemi, and N. Phan, "Significance of hot isostatic pressing (HIP) on multiaxial deformation and fatigue behaviors of additive manufactured Ti-6Al-4V including build orientation and surface roughness effects," *International Journal of Fatigue*, vol. 117, pp. 352–370, Dec. 2018, doi: 10.1016/j.ijfatigue.2018.07.035.

[37] R. Molaei, A. Fatemi, and N. Phan, "Multiaxial fatigue of LB-PBF additive manufactured 17–4 PH stainless steel including the effects of surface roughness and HIP treatment and comparisons with the wrought alloy," *International Journal of Fatigue*, vol. 137, p. 105646, Aug. 2020, doi: 10.1016/j.ijfatigue.2020.105646.

[38] N. Sanaei and A. Fatemi, "Analysis of the effect of surface roughness on fatigue performance of powder bed fusion additive manufactured metals," *Theoretical and Applied Fracture Mechanics*, vol. 108, p. 102638, Aug. 2020, doi: 10.1016/j.tafmec.2020.102638.

[39] J. P. Oliveira, A. D. LaLonde, and J. Ma, "Processing parameters in laser powder bed fusion metal additive manufacturing," *Materials & Design*, vol. 193, p. 108 762, Aug. 2020.

[40] F42 Committee, "Additive manufacturing Test artifacts Geometric capability assessment of additive manufacturing systems," *ASTM International, Tech. Rep.*

[41] A. Reichardt, A. A. Shapiro, R. Otis, R. P. Dillon, J. P. Borgonia, B. W. McEnerney, P. Hosemann, and A. M. Beese, "Advances in additive manufacturing of metal-based functionally graded materials," *International Materials Reviews*, vol. 66, no. 1, pp. 1–29, Jan. 2021.

[42] M. A. Obeidi, "Metal additive manufacturing by laser-powder bed fusion:Guidelines for process optimisation," *Results in Engineering*, vol. 15, p. 100473, Sep. 2022

[43] L. Johnson, M. Mahmoudi, B. Zhang, R. Seede, X. Huang, J. T. Maier, H. J. Maier, I. Karaman, A. Elwany, and R. Arr´oyave, "Assessing printability maps in additive manufacturing of metal alloys," *Acta Materialia*, vol. 176, pp. 199–210, Sep. 2019.

[44] A. Dass and A. Moridi, "State of the Art in Directed Energy Deposition: From Additive Manufacturing to Materials Design," *Coatings*, vol. 9, no. 7, p. 418, Jul. 2019.

[45] S. M. Yusuf and N. Gao, "Influence of energy density on metallurgy and properties in metal additive manufacturing," *Materials Science and Technology*, vol. 33, no. 11, pp. 1269–1289, Jul. 2017.

[46] S. Islam *et al.*, "Quantitative ultrasonic characterization of subsurface inclusions in tapered roller bearings: 12th Symposium on Bearing Steel Technologies: Progress in Bearing Steel Metallurgical Testing and Quality Assurance," *Bearing Steel Technologies*, pp. 66–81, 2020, doi: 10.1520/STP162320190081.

[47] C. M. Tarawneh, J. A. Turner, L. Koester, and B. M. Wilson, "Service Life Testing of Railroad Bearings with Known Subsurface Inclusions: Detected with Advanced Ultrasonic Technology," *Int J Railw Tech*, vol. 2, no. 3, pp. 55–78, 2013

[48] B. M. Wilson, A. J. Fuller, C. Tarawneh, and J. A. Turner, "Near race inclusions in bearing components and the resultant effect on fatigue initiation and component life," *CORE 2016: Maintaining the Momentum*, pp. 697–702, doi: 10.3316/informit.437537875310649.

[49] Z. Smoqi, J. Toddy, H. (Scott) Halliday, J. E. Shield, and P. Rao, "Process-structure relationship in the directed energy deposition of cobalt-chromium alloy (Stellite 21) coatings," *Materials & Design*, vol. 197, p. 109229, Jan. 2021

[50] L.E. Levine, B. Lane, "Additive Manufacturing Benchmark Test Series, AMB2018-01 Description," National Institute of Standards and Technology (2019), available at: https://www.nist.gov/ambench/amb2018-01-description.

[51] C. A. Schneider, W. S. Rasband, and K. W. Eliceiri, "NIH Image to ImageJ: 25 years of image analysis," *Nature Methods* 9, 671–675 (2012). doi:10.1038/nmeth.2089

[52] Z. Y. Liu, C. Li, X. Y. Fang, and Y. B. Guo, "Energy Consumption in Additive Manufacturing of Metal Parts," *Procedia Manufacturing*, vol. 26, pp. 834–845, Jan. 2018

[53] A. Spierings, M. Schneider, and R. Eggenberger, "Comparison of Density Measurement Techniques for Additive Manufactured Metallic Parts," *Rapid Prototyping Journal* 17, 380–386 (2011). doi:10.1108/13552541111156504

[54] L. D. Sotelo, H. Hadidi, C. S. Pratt, M. P. Sealy, and J. A. Turner, "Ultrasonic mapping of hybrid additively manufactured 420 stainless steel," *Ultrasonics*, vol. 110, p. 106269, Feb. 2021

[55] G. Ghoshal and J. A. Turner, "Diffuse ultrasonic backscatter at normal incidence through a curved interface," *The Journal of the Acoustical Society of America*, vol. 128, no. 6, pp. 3449–3458, Dec. 2010, doi: 10.1121/1.3500683.